



Ultra-low platinum loadings in polymer electrolyte membrane fuel cell electrodes fabricated *via* simultaneous electrospinning/electrospraying method



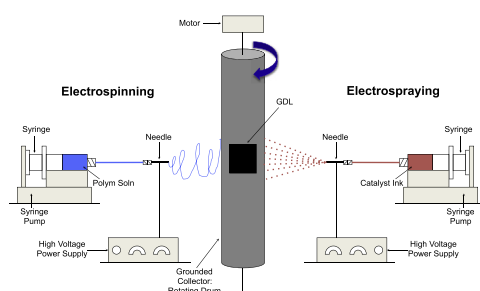
Xuhai Wang, Francis W. Richey, Kevin H. Wujcik, Yossef A. Elabd*

Department of Chemical and Biological Engineering, Drexel University, Philadelphia, PA 19104, United States

HIGHLIGHTS

- New electrospinning/electrospraying technique developed for fuel cell electrodes.
- Unique nanoparticle/nanofiber electrode morphology evidenced by microscopy.
- Ultra-low platinum loadings at high power densities were observed.
- Excellent platinum utilization of 0.024 g_{Pt} kW⁻¹ was achieved.
- High electrochemical surface area was measured by cyclic voltammetry.

GRAPHICAL ABSTRACT



ARTICLE INFO

Article history:

Received 19 January 2014

Received in revised form

28 March 2014

Accepted 11 April 2014

Available online 24 April 2014

Keywords:

Electrospinning

Nanofiber

Fuel cell

Nafion

Platinum

Hydrogen

ABSTRACT

In this study, membrane electrode assemblies (MEAs) were fabricated using a simultaneous electrospinning/electrospraying (E/E) technique to produce a unique nanoparticle/nanofiber cathode catalyst layer morphology evidenced by scanning electron microscopy. H₂/O₂ and H₂/air polymer electrolyte membrane fuel cell performance was evaluated for E/E MEAs at ultra-low Pt cathode loadings of 0.052 and 0.022 mg_{Pt} cm⁻², where maximum power densities of 1.090 and 0.936 W cm⁻² (H₂/O₂) and 0.656 and 0.625 W cm⁻² (H₂/air) were achieved at these two Pt loadings, respectively. This was compared to a conventional control MEA at a 0.42 mg_{Pt} cm⁻² cathode catalyst loading with maximum power densities of 1.420 and 0.839 W cm⁻² for H₂/O₂ and H₂/air, respectively. These results correspond to a significant reduction in Pt loading (5–12% of control) at only a modest reduction in power density (~66–78% of control) for the E/E electrodes. Excellent platinum utilization in the cathode of 0.024 g_{Pt} kW⁻¹ (~42 kW g_{Pt}⁻¹) was achieved for the E/E electrode at 0.022 mg_{Pt} cm⁻² cathode loading. Cyclic voltammetry results show an electrochemical surface area higher in the E/E electrodes compared to the control, which provides a rationale for the excellent platinum utilization results, where the E/E morphology results in more triple phase boundaries with more accessible Pt in the electrode.

© 2014 Elsevier B.V. All rights reserved.

1. Introduction

Proton exchange membrane (PEM) fuel cells have attracted considerable interest as alternative power sources for large market

applications, such as transportation (hydrogen-fueled PEM fuel cell vehicles). This is because of their high efficiency, high energy and power density, low-to-moderate-temperature operation, rapid start-up time, with fuels from renewable sources with zero point-of-use green house gas emissions. In addition, research and development over the past several decades has contributed to advancements that overcome many of the major hurdles to bringing fuel cell vehicles to the market place, such as durability, reliability,

* Corresponding author.

E-mail address: elabd@drexel.edu (Y.A. Elabd).

lifetime performance, safety, and fuel storage. However, platinum (Pt), a rare precious metal, which is the most active catalyst for PEM fuel cells, is still a major factor that has limited the mass commercialization of fuel cell vehicles, where Pt contributes to a significant portion of the fuel cell engine cost [1,2]. Attempts to reduce this cost have led to research in alternative catalyst materials and alternative electrode designs.

First generation PEM fuel cells utilized un-supported Pt, which required high Pt loadings to achieve reasonable power densities [3]. Initial reductions in Pt loading in regards to alternative catalysts were achieved through the dispersion of Pt nanoparticles on high surface area carbon supports (Pt/C), i.e., supported Pt [1,4,5]. Other alternative catalyst materials that have been explored include non-noble metals, Pt alloys, Pt core–shell structures, and Pt supported thin films [6–10]. Early research on electrode design demonstrated that a significant reduction (approximately an order of magnitude) could be achieved by introducing the Nafion ionomer into the electrode [11]. These lower Pt loadings were achieved by increasing the triple phase boundary (TPB), which are the junction points where catalytic and electron conduction sites, reactant gases (pores), and proton conducting Nafion ionomer meet. Others have observed performance enhancements and reduced Pt loadings without significant performance loss through adjustments to this Nafion ionomer content in the electrodes [12–17]. More recently, alternative electrode designs have been explored with the attempt to expose more Pt surface area for the oxygen reduction reaction (ORR) and increase the TPB. Examples include electrospinning [18–21] and electrospinning [22,23] catalyst/ionomer mixtures to produce electrodes. Specifically, recent results from Pintauro and co-workers [22,23] demonstrate high PEM fuel cell power output with significantly lower Pt loadings compared to conventional electrodes.

Electrospinning is an intriguing approach to fabricate fuel cell electrodes. Previous results from our laboratory revealed the discovery of the natural formation of Nafion nanofibers in fuel cell electrodes with a careful *post mortem* (after fuel cell experiment) microscopy investigation [24]. A ~10% fuel cell performance improvement was observed specifically due to the formation of Nafion nanofibers, where only a small fraction of the Nafion ionomer were in nanofiber form [24]. These results suggest that Nafion nanofibers increase the TPB and designing fuel cell electrodes with higher Nafion nanofiber content may result in high power density fuel cells with much lower Pt loadings. Electrospinning is a technique that can produce high fidelity polymer nanofibers at high production rates. The production of Nafion nanofibers *via* electrospinning has previously been demonstrated by our laboratory and others [25–28]. Interestingly, the single Nafion nanofiber properties exhibit super high proton conductivity (as high as 1.5 S cm^{-1}), which is an order of magnitude higher than Nafion bulk films ($\sim 0.1 \text{ S cm}^{-1}$) [26]. The proton conductivity in single Nafion nanofibers increased exponentially with decreasing fiber diameter, where an oriented ionic nanostructure was observed in the axial direction of these fibers with small-angle X-ray scattering and provides the rationale for the enhanced conductivity [26]. These results motivate further investigation into Nafion nanofibers and the design of Nafion nanofiber-based electrodes for fuel cells.

In this study, electrospinning and electrospaying were combined in a simultaneous process to produce cathode catalyst layers for PEM fuel cells. Specifically, Nafion nanofibers and Pt/C nanoparticles were introduced separately and simultaneously by two different needles (see Fig. 1) using electrospinning and electrospaying, respectively, to produce unique nanoparticle/nanofiber electrodes. This electrospinning/electrospaying (E/E) technique differs from electrospinning or electrospaying alone, where a

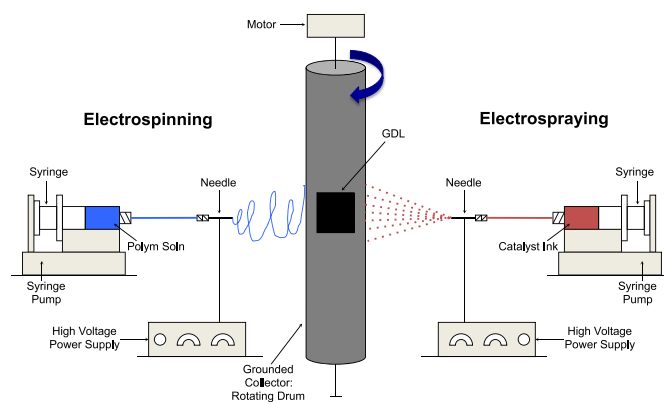


Fig. 1. Schematic of simultaneous electrospinning/electrospaying (E/E) two-needle system.

mixture of Nafion and Pt/C are expelled from the same needle. This E/E technique allows for a higher level of control over fiber size and Pt loading compared to other electrode fabrication techniques. In this paper, the cathode layers and subsequently membrane electrode assemblies (MEAs) were fabricated using the E/E technique and the morphology, fuel cell performance, and electrochemical surface area were investigated as a function of Pt loading and compared to MEAs fabricated with conventional electrodes.

2. Experimental

2.1. Materials

Isopropanol (99.5%, Sigma–Aldrich), ethanol (99.5%, Decon Labs, Inc., 99.5%), Nafion solution (1000 EW, 5 wt% in a 3/1 v/v of isopropanol/water, Ion Power), poly(acrylic acid) (PAA; $M_v = 450,000 \text{ g mol}^{-1}$, Aldrich), 20 wt% Pt on carbon catalyst (Pt/C; Vulcan XC-72, Premetek Co.), gas diffusion layer (GDL; SGL-25BC, Fuel Cells Etc.), and Nafion NR-212 membrane (1100 EW, $\sim 50 \mu\text{m}$ (0.002 in) dry thickness, Ion Power) were used as received. Ultra-pure deionized (DI) water with resistivity $\sim 16 \text{ M}\Omega \text{ cm}$ was used as appropriate. Ultra high purity grade N_2 , H_2 , O_2 and ultra zero grade air were all purchased from airgas and used for all fuel cell experiments.

2.2. Two-needle electrospinning/electrospaying (E/E) system

Fig. 1 shows a schematic diagram of the simultaneous E/E apparatus used in this study. The custom-designed apparatus consists of two high-voltage power supplies (Model PS/EL50R00.8, Glassman High Voltage, Inc. and Model ES40P-10W/DAM, Gama High Voltage Research), two syringe pumps (Model NE-1000, New Era Pump Systems), two syringe needles (i.d. = 0.024 in., Hamilton), tubing (Pt. No. 30600-65, Cole–Parmer), and a grounded collector (aluminum foil coated cylindrical drum, o.d. = 4.85 cm). The collector drum is connected to a motor (Model 41K25GN-SW2, Oriental Motor) to allow for rotation during the E/E process, where the rotational speed was set to 100 rpm. A GDL was adhered to the collector drum, where nanofibers/nanoparticles could be directly collected *via* the E/E process, where catalyst ink is electrospayed and polymer solution is electrospun simultaneously. Details regarding catalyst ink and polymer solution preparation are described in the following section. The needle tip to collector distances, applied voltages, and solution flow rates were 15 and 9 cm, 10.5 and 12.5 kV, and 0.3 and 3 ml h^{-1} for the electrospinning and electrospaying processes, respectively.

2.3. Membrane electrode assembly (MEA)

Catalyst ink used in the electrospraying portion of the E/E electrodes consisted of 20 mg Pt/C catalyst, 0.248 ml DI water, 0.043 ml Nafion solution, 0.171 ml isopropanol/water (3/1 v/v), and 1.970 ml ethanol. This mixture was sonicated for 3 min (Model CL-18, Qsonica Sonicator) prior to electrospraying. The mixture corresponds to 10/1 wt/wt (Pt/C)/Nafion, which is five times higher in Pt/C content than the catalyst ink prepared for hand-painted electrodes (control) as described below. Less Nafion is required for electrospraying, because Nafion is also supplied from electrospinning to produce the E/E electrode. Therefore, the final (Pt/C)/Nafion ratio in the E/E electrode is similar to the hand-painted electrode, when one accounts for the Nafion from both electrospraying and electrospinning. The polymer solution used in the electrospinning portion of the E/E electrodes consisted of 4/1 wt/wt Nafion/PAA. A 5 wt% polymer (PAA and Nafion) solution was prepared by combining 131.1 mg PAA, 10,494 mg Nafion solution, and 2491.7 mg isopropanol/water (3/1 v/v). This solution was stirred at ~ 70 – 80 °C for ~ 12 h to ensure complete dissolution. The solution was cooled down to ambient temperature before electrospinning. The catalyst ink and the polymer solution were used to make E/E electrodes as described in the previous section. After the E/E process, the E/E electrodes were annealed at 135 °C for 5 min.

The catalyst ink used to prepare hand-painted electrodes (control sample) was prepared by mixing 100 mg solid Pt/C catalyst, 550 mg DI water, 1000 mg Nafion solution, and 1350 mg IPA via sonication for 3 min. This mixture corresponds to 2/1 wt/wt (Pt/C)/Nafion and 3/1 v/v isopropanol/water.

MEAs were fabricated by sandwiching the Nafion NR-212 membrane between two catalyst-coated GDLs (anode and cathode catalyst layers) and hot pressing (heat press, Carver) for 5 min at 135 °C and 1.5 MPa (213 psi). Cathode catalyst layers consisted of either hand-painted GDLs (control) or E/E GDLs at various Pt loadings. All anode catalyst layers in this study were hand painted with a Pt loading of 0.15 mg cm⁻².

2.4. Electrode characterization

Morphological characterization of the E/E electrode was investigated with scanning electron microscopy (SEM, Model FEI/Philips XL-30, 10 kV). SEM images of the E/E electrode were collected after electrospinning/electrospraying of the nanofibers/nanoparticles on the GDL, but before MEA fabrication. SEM images were also collected after fuel cell tests (*post mortem*), where cross sectional views of MEAs were analyzed, which were prepared by freeze fracturing the MEAs. All samples were sputter coated (Denton Desk II Sputtering System) with platinum at 40 mA for 30 s before SEM analysis. The diameter of nanofibers and nanoparticles were measured using ImageJ software by counting 30 randomly selected fibers and particles for each SEM image.

The Pt loading was measured with thermal gravimetric analysis (TGA; TGA 7, Perkin Elmer). A small portion of the E/E electrode (~ 5 – 7 mg) was heated in the TGA from ambient temperature to 900 °C at 5 °C min⁻¹ in air at 20 ml min⁻¹. Since all components in E/E electrode volatilize above 900 °C with the exception of Pt, the Pt loading was determined by comparing the weight of the E/E electrode before and after exposure to 900 °C in the TGA.

2.5. Fuel cell tests and cyclic voltammetry (CV)

Each MEA (1.21 cm² area) was placed between two serpentine flow field graphite plates (1 cm² flow area) separated by two 0.160 mm thick Teflon coated gaskets (Pt No. 381-6, Saint Gobian). The entire fuel cell assembly consisted of an MEA, two gaskets, and

two flow plates placed between two copper electrodes followed by endplates all held together by tie rods (bolts) with 11.3 N·m (100 lb-in) of torque. The fuel cell performance (polarization curves: voltage vs. current density) of each MEA was evaluated with a Fuel Cell Test Station (850C, Scribner Associates, Inc.). Fuel cell tests were conducted at both ambient and 172 kPa (25 psi) of back pressure with saturated (RH = 100%) anode and cathode flow rates of 0.42 L min⁻¹ hydrogen and 1.0 L min⁻¹ air, respectively. The cathode, anode, and cell were all maintained at 80 °C. Polarization curves were collected from open circuit voltage (OCV) to 0.2 V at increments of 0.05 V min⁻¹. The fuel cell performance was recorded after a new MEA was fully activated. The activation process included operating an MEA at 0.7 V for ~ 1 – 2 h followed by voltage scanning from OCV to 0.2 V several times. This activation process was repeated until the MEA reached steady state and no further increase in current was observed when the fuel cell was held at constant voltage. The activation process typically occurs over 4–6 h before the MEA reached a steady state condition.

Cyclic voltammetry (CV) was performed on a two-electrode MEA with a potentiostat (Solartron SI 1287, Corrware Software) at 20 mV s⁻¹ from 0 to 1.2 V. In this configuration, the anode serves as both the counter and reference electrodes. The fuel cell anode and cathode were supplied with 0.040 L min⁻¹ H₂ and 0.018 L min⁻¹ N₂, respectively. Temperatures of the cathode, anode and cell were maintained at 30 °C. The Pt catalyst was assumed to have an average site density of 210 $\mu\text{C cm}^{-2}$ [29]. The electrochemical surface area (ECSA) was determined from the hydrogen adsorption area from 0.1 to 0.4 V of the CV data.

3. Results and discussion

Fig. 2 shows SEM images of E/E electrodes prior to MEA fabrication along with nanofiber diameter and nanoparticle diameter size distributions. Specifically, Fig. 2(a) shows an SEM image of an E/E electrode with 0.022 mg cm⁻² Pt cathode loading and Fig. 2(b) shows a magnified view of Fig. 2(a). Fig. 2(a) shows that the E/E electrode is highly porous and fairly uniform over a large length scale (~ 10 μm). The high porosity should improve gas transport throughout the electrode from the gas flow channel to the catalyst layer, while the continuously connected network nanofibers and nanoparticles should increase the triple phase boundary, which requires intimate junction points for combined ORR, proton and electron transport. Several large catalyst agglomerates (1–2 μm) were observed in Fig. 2(b), however, the majority were in the 50–300 nm size range as evidenced in Fig. 2(d). Although the size of some of the agglomerates is large compared to discrete nanoparticles, the surfaces of these agglomerates are fairly rough and porous, which should allow for minimal gas transport and ORR resistance. Fig. 2(c) shows a uniform nanofiber diameter size distribution of ~ 200 nm. The nanoparticle diameter size distribution is broader than the nanofiber size distribution with $\sim 20\%$ of the nanoparticles with diameters over 450 nm. Nanoparticle agglomerate size is important as surface area affects the effective ORR and subsequently fuel cell performance.

Fig. 2(e) shows an SEM image of an E/E electrode with a higher Pt cathode loading (0.052 mg cm⁻²) and Fig. 2(f) shows a magnified view of Fig. 2(e). A higher number of catalyst agglomerates were observed in Fig. 2(e) compared to the E/E electrode with lower Pt loading shown in Fig. 2(a). The diameter distributions of the nanoparticles and nanofibers in Fig. 2(g) and (h) show that the fiber sizes are similar to those in Fig. 2(c), but the particle sizes are different from those in Fig. 2(d). The electrospraying flow rate (3 ml h⁻¹) was set higher than the electrospinning flow rate (0.3 ml h⁻¹) in order to achieve a desired (Pt/C)/Nafion ratio (2/1) in the catalyst layer, while Pt loading was controlled by the duration of

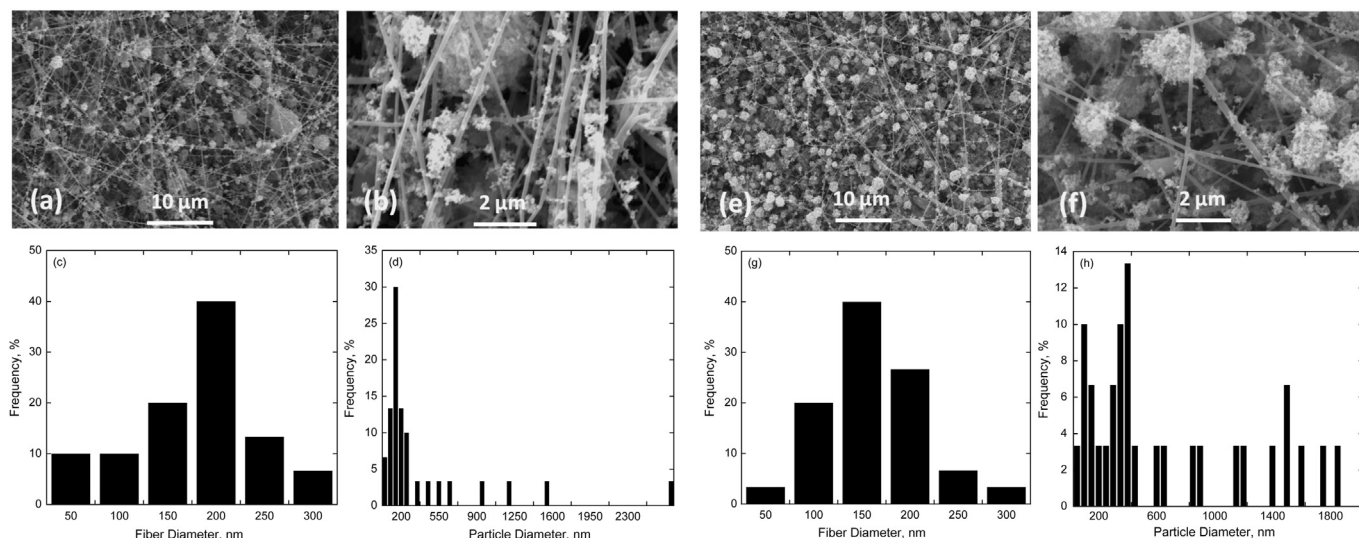


Fig. 2. (a) SEM image of E/E electrode with 0.022 mg cm^{-2} Pt loading, (b) higher magnification of (a), nanofiber diameter (c) and nanoparticle diameter (d) size distributions, (e) SEM image of E/E electrode with 0.052 mg cm^{-2} Pt loading, (f) higher magnification of (e), nanofiber diameter (g) and nanoparticle diameter (h) size distributions.

the E/E process. This difference in flow rates may result in higher particle agglomerate sizes at higher loadings, while not significantly affecting fiber sizes. Additionally, slight changes in environmental conditions (e.g., temperature, relative humidity) may affect electrospinning more than electrospinning.

Fuel cell performances for the E/E electrodes at both Pt cathode loadings (0.022 and 0.052 mg cm^{-2}), as well as the hand-painted electrode (control) at a 0.42 mg cm^{-2} Pt cathode loading, are

shown in Fig. 3 for H_2/air and H_2/O_2 with and without back pressure. Maximum power density for each experiment is listed in Table 1. Fig. 3(a) shows the H_2/O_2 fuel cell performance at 172 kPa back pressure (273 kPa absolute pressure) on anode and cathode sides, respectively. A maximum power density of 1.420 , 1.090 , and 0.936 W cm^{-2} were measured at Pt cathode loadings of 0.42 (control), 0.052 (E/E), and 0.022 (E/E) mg cm^{-2} , respectively. This corresponds to a 77% and 66% maximum power output at only a

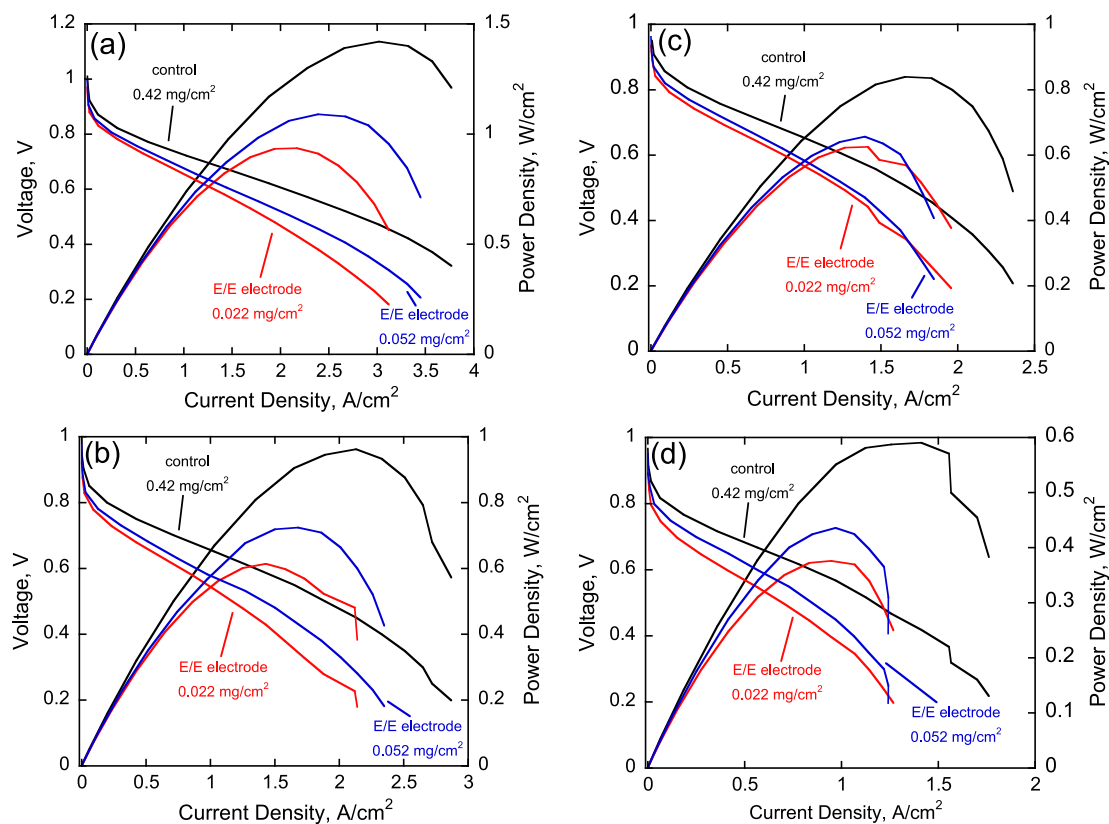


Fig. 3. Fuel cell performance of the E/E electrodes and the hand-painted electrodes (control) with operating conditions of (a) H_2/O_2 with 25 psi back pressure, (b) H_2/O_2 at ambient pressure, (c) H_2/air with 25 psi back pressure, (d) H_2/air at ambient pressure.

Table 1
Fuel cell performance of MEAs with E/E cathodes.

Fuel cell conditions	Peak power, W cm ⁻²		
	E/E cathode 0.022 mg _{Pt} cm ⁻²	E/E cathode 0.052 mg _{Pt} cm ⁻²	Control cathode 0.420 mg _{Pt} cm ⁻²
H ₂ /O ₂ /bp ^a	0.936	1.090	1.420
H ₂ /O ₂ /no bp	0.614	0.724	0.962
H ₂ /air/bp	0.625	0.656	0.839
H ₂ /air/no bp	0.373	0.434	0.590

^a bp = back pressure of 172 kPa (25 psi).

Table 2
Platinum utilization and electrochemical surface area of MEAs with E/E cathodes.

Cathode type	Cathode loading, mg _{Pt} cm ⁻²	Pt utilization at maximum power, g _{Pt} kW ^{-1a}	Pt utilization at maximum power, g _{Pt} kW ^{-1b}	ECSA ^c , m ² g _{Pt} ⁻¹
E/E	0.022	0.024	0.059	93.9
E/E	0.052	0.048	0.119	86.8
Control	0.420	0.296	0.712	53.2

^a H₂/O₂/bp.

^b H₂/air/no bp.

^c ECSA = electrochemical surface area.

12% and 5% Pt loading for the E/E electrodes at 0.052 and 0.022 mg cm⁻² Pt cathode loadings, respectively, compared to the control (hand-painted 0.42 mg cm⁻² Pt cathode loading). These results indicate that the E/E electrodes are highly effective at improving the fuel cell performance at ultra-low Pt loadings and suggest an increase in the triple phase boundary.

As expected, when the back pressure is removed, as shown in Fig. 3(b), the maximum power output for the control experiment (0.42 mg cm⁻² Pt cathode loading) lowers from 1.420 to 0.962 W cm⁻² and the voltage decreases, specifically at higher current densities. However, the comparisons between the control and the E/E electrodes are similar to the results with back pressure, where a 75% (0.724 W cm⁻²) and 64% (0.614 W cm⁻²) maximum power output for the E/E electrodes at 0.052 and 0.022 mg cm⁻² Pt cathode loading, respectively, compared to the control (0.42 mg cm⁻² Pt) was observed.

Fig. 3(c) and (d) shows the H₂/air fuel cell performance with and without back pressure, respectively. As expected the power density for H₂/air is lower than H₂/O₂. However, the comparisons between the control and the E/E electrodes are similar for H₂/air as was observed for H₂/O₂ fuel cell results. For H₂/air with back pressure (Fig. 3(c)), a 78% (0.656 W cm⁻²) and 74% (0.625 W cm⁻²) maximum power output for the E/E electrodes at 0.052 and 0.022 mg cm⁻² Pt cathode loading, respectively, compared to the control at 0.42 mg cm⁻² Pt cathode loading (0.839 W cm⁻²) was observed. For H₂/air without back pressure (Fig. 3(d)), a 74% (0.434 W cm⁻²) and 63% (0.373 W cm⁻²) maximum power output for the E/E electrodes at 0.052 and 0.022 mg cm⁻² Pt cathode loading, respectively, compared to the control at a 0.42 mg cm⁻² Pt cathode loading (0.590 W cm⁻²) was observed.

It is clear from Fig. 3 that the fuel cell performance increases with Pt loading, however, the control electrode requires extraordinarily higher Pt loading to overpass the performance of the E/E electrode. The unique nanofiber/nanoparticle morphology of the E/E electrode allows for high PEM fuel cell performance at ultra low Pt loadings.

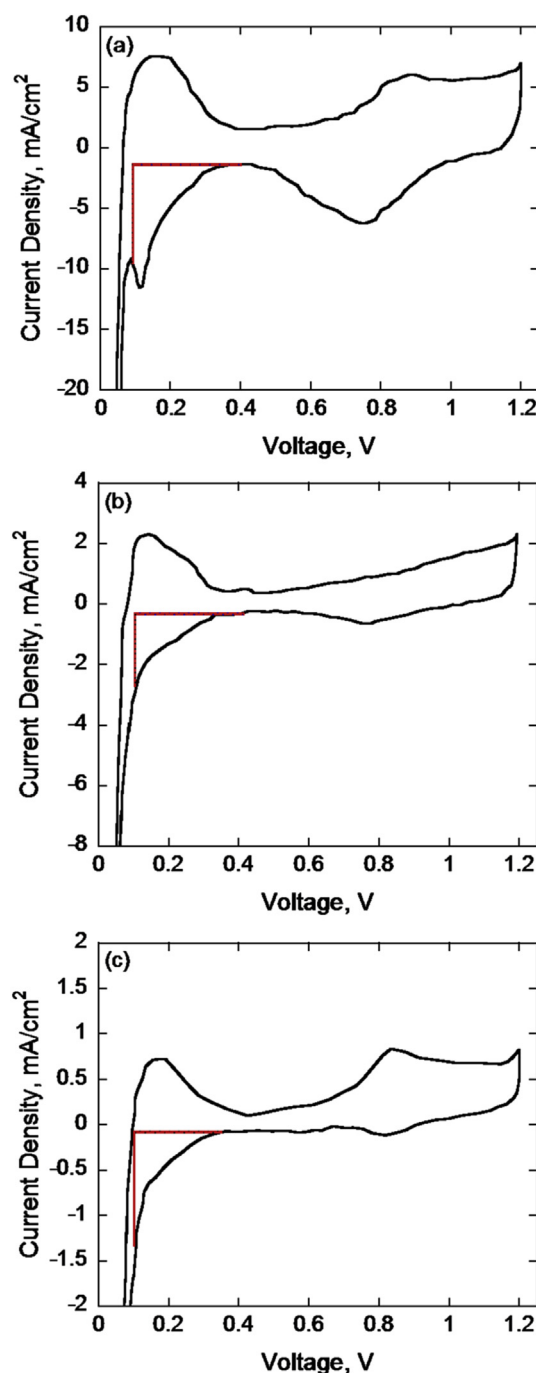


Fig. 5. Cyclic voltammograms of (a) MEA with hand-painted electrodes (control) with Pt cathode loading of 0.420 mg cm⁻² and of MEAs with E/E electrodes at Pt cathode loadings of (b) 0.052 mg cm⁻² and (c) 0.022 mg cm⁻². Boxed area was used to determine the ECSA.

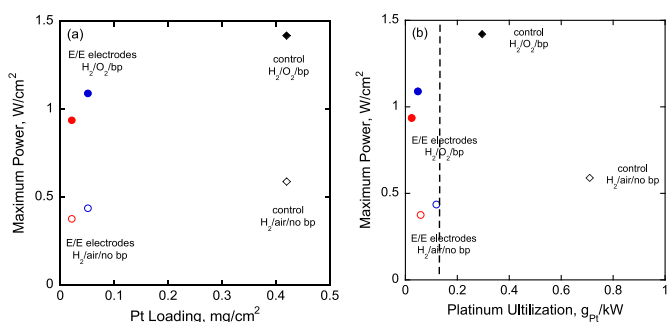


Fig. 4. Maximum fuel cell power output for H₂/O₂ with 25 psi back pressure and H₂/air at ambient pressure versus (a) Pt loading and (b) Pt utilization. Dashed line corresponds to 2015 DOE platinum utilization target.

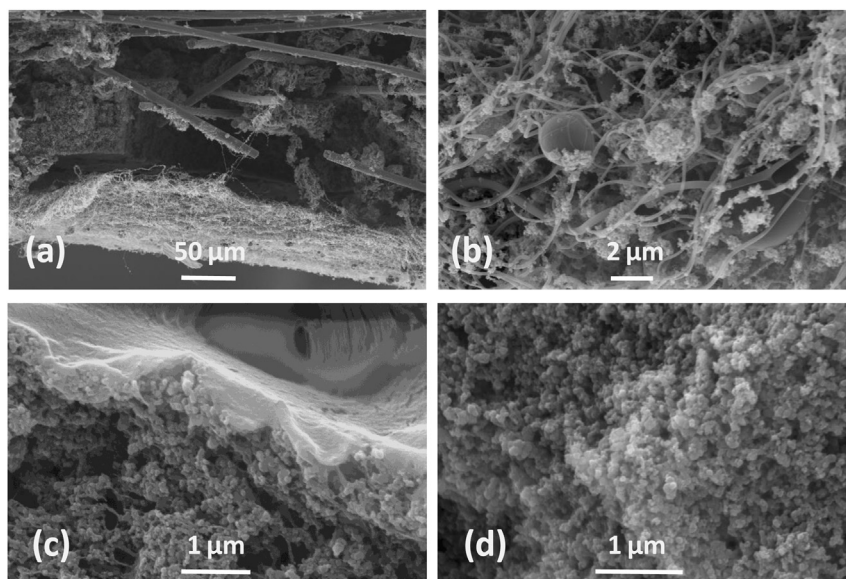


Fig. 6. Freeze-fractured cross-section SEM images of (a) E/E electrode at 0.022 mg cm^{-2} Pt loading after electrospinning/electrospraying and before hot-compression, (b) higher magnification of (a), (c) *post mortem* SEM images of (a) and (d) control cathode at 0.42 mg cm^{-2} Pt loading.

Fig. 4 and Tables 1 and 2 shows the maximum fuel cell power output for the E/E and control cathodes as a function of Pt cathode loading and Pt utilization for H_2/O_2 with back pressure and H_2/air without back pressure operating conditions. For H_2/O_2 with back pressure conditions, a 19-fold reduction in Pt loading for the E/E electrode (0.022 mg cm^{-2}) at the high power density of 0.936 W cm^{-2} corresponds to a cathode platinum utilization of $0.024 \text{ g}_{\text{Pt}} \text{ kW}^{-1}$, which is over an order of magnitude lower than the control ($0.296 \text{ g}_{\text{Pt}} \text{ kW}^{-1}$). For the H_2/air without back pressure, this same reduction in Pt loading for the E/E electrode (0.022 mg cm^{-2}) corresponds to a cathode platinum utilization of $0.059 \text{ g}_{\text{Pt}} \text{ kW}^{-1}$ at a power density of 0.373 W cm^{-2} , which is also over an order of magnitude lower than the control ($0.712 \text{ g}_{\text{Pt}} \text{ kW}^{-1}$). For H_2/O_2 without back pressure and H_2/air with back pressure conditions, a cathode platinum utilization of 0.036 and $0.035 \text{ g}_{\text{Pt}} \text{ kW}^{-1}$, respectively, for the E/E electrode at 0.022 mg cm^{-2} Pt cathode loading was observed, which were both over an order of magnitude lower compared to the control ($0.437 \text{ g}_{\text{Pt}} \text{ kW}^{-1}$ and $0.501 \text{ g}_{\text{Pt}} \text{ kW}^{-1}$, respectively; not shown in Table 2).

Although the control cathode with Pt loading of 0.42 mg cm^{-2} resulted in the highest output power density, the platinum utilization is not optimal, and the cost of a fuel cell stack would be cost prohibitive. Overall, for all fuel cell operating conditions, the E/E electrodes resulted in a 63–78% power output at only 5–12% of the Pt cathode loading compared to the control. This corresponds to platinum utilization for the E/E electrodes at all fuel cell operating conditions lower than the U.S. Department of Energy 2015 target ($0.125 \text{ g}_{\text{Pt}} \text{ kW}^{-1}$) [30], which would correspond to a significant reduction in fuel cell stack cost with only a minor loss in power density. It is important to also note that the E/E electrodes have not yet been fully optimized. Optimization of the E/E process and E/E electrode morphology could result in higher fuel cell performance at even lower Pt loadings.

To further understand the impact of the electrode morphology on the triple phase boundary and the subsequent fuel cell performance, cyclic voltammetry was performed to determine the electrochemical surface area (ECSA). Fig. 5 shows the cyclic voltammograms (CVs) of the all the MEAs in this study, where the ECSAs were determined from integrating the hydrogen adsorption

regions from 0.1 to 0.4 V. CVs were performed on both E/E MEAs and compared to the control. Table 2 lists the results, where ECSAs of 93.9, 86.8, and $53.2 \text{ m}^2 \text{ g}_{\text{Pt}}^{-1}$ were measured for the Pt cathode loadings of 0.022 mg cm^{-2} (E/E), 0.052 mg cm^{-2} (E/E), and 0.42 mg cm^{-2} (control), respectively. The E/E electrodes show an improvement in ECSA compared to the control and ECSA appears to increase with decreasing Pt loading in the E/E electrode. In addition to the SEM images, the CV data provides further rationale for the low Pt utilization at high fuel cell power densities in E/E electrodes.

Fig. 6(a) shows the freeze-fractured cross-section SEM image of the E/E electrode at a Pt loading of 0.022 mg cm^{-2} . The lower and upper sections in Fig. 6(a) clearly show the E/E catalyst layer and the gas diffusion layer, respectively, where the thickness of the E/E electrode is approximately several micrometers. Fig. 6(b) shows a higher magnification image of Fig. 6(a). Fig. 6(c) and (d) show the *post mortem* SEM images of the E/E and control cathodes, respectively. The upper right corner of Fig. 6(c) is the Nafion membrane. As shown in Fig. 6(c), only a few fibers are visible in the E/E catalyst layer after the fuel cell test. When Fig. 6(c) is compared to Fig. 6(b) or Fig. 2, many fibers, particularly larger fibers, are no longer visible. However, nanofibers are still present in Fig. 6(c). Compression at higher temperatures either during MEA fabrication or fuel cell experiments clearly alters the cathode morphology, where a redistribution of fibers and catalyst particles is evident when comparing to Fig. 6(b) or Fig. 2. The compaction of particles and fibers may actually improve electrical and proton conductivity, respectively, via improved particle and fiber connectivity. Regardless of the altered morphology when comparing Fig. 6(c) to Fig. 2, there are apparent differences in the *post mortem* morphology when comparing the E/E cathode (Fig. 6(c)) to the control cathode (Fig. 6(d)). The E/E cathode appears to have a higher porosity than the control and also contains Nafion nanofibers. Although no Nafion nanofibers are evident in the *post mortem* SEM image of the control cathode, one should note that the natural formation of Nafion nanofibers have been previously observed in conventionally fabricated fuel cell electrodes after exposure to fuel cell environments [24]. However, these fibers are not uniformly distributed throughout fuel cell electrodes. It appears that there may be an

overall higher uniformity in higher porosity and appearance of Nafion nanofibers in E/E electrodes compared to conventional electrodes, and therefore results in improved Pt utilization and high power densities. These results clearly warrant future work that would focus on a more comprehensive morphology characterization of E/E electrodes before and after fuel cell experiments. It is clear that nanofibers play an important role in the redistribution and formation of the porous catalyst layer in the E/E electrode. The fuel cell performance can possibly be further improved by electrospinning nanofibers that remain in their fiber form after MEA fabrication and fuel cell tests. A more comprehensive investigation, including various fuel cell operating conditions, long-term performance, and various MEA sizes, is currently underway.

4. Conclusions

The simultaneous electrospinning/electrospraying process is a new technique that produces unique nanoparticle/nanofiber electrodes for fuel cells. Separating the electrospinning and electro-spraying process provides a higher level of control over Nafion fiber diameters and Pt/C agglomerate sizes and subsequently the overall electrode morphology. This provides an excellent platform to investigate the impact of electrode morphology on the triple phase boundary and power output/Pt loading relationships, i.e., platinum utilization. In this study, the E/E technique was demonstrated for the first time to explore this new electrode morphology and the impact of Pt loading on PEM fuel cell performance. An order of magnitude improvement in Pt utilization was observed with E/E electrodes compared to control electrodes with an order of magnitude lower Pt loadings with only modest reductions in power output. The E/E morphology and electrochemical surface area measured by electron microscopy and cyclic voltammetry, respectively, provide a rationale for the observed results. Understanding the power/loading relationship boundaries with future optimization of E/E electrodes would be of significant interest.

Acknowledgments

This work is supported in part by the Energy Commercialization Institute under grant no. DUETRF-5.

References

- [1] H.A. Gasteiger, S.S. Kocha, B. Sompalli, F.T. Wagner, *Appl. Catal. B Environ.* 56 (2005) 9–35.
- [2] J. Spendelov, J. Marcinkoski, DOE Fuel Cell Technologies Program Record, Record No. 12020, 2012.
- [3] J. Marcinkoski, B.D. James, J.A. Kalinoski, W. Podolski, T. Benjamin, J. Kopasz, *J. Power Sources* 196 (2011) 5282–5292.
- [4] T.R. Ralph, G.A. Hards, J.E. Keating, S.A. Campbell, D.P. Wilkinson, M. Davis, J. StPierre, M.C. Johnson, *J. Electrochem. Soc.* 144 (1997) 3845–3857.
- [5] M.S. Wilson, S. Gottesfeld, *J. Electrochem. Soc.* 139 (1992) L28–L30.
- [6] R. Othman, A.L. Dicks, Z.H. Zhu, *Int. J. Hydrogen Energy* 37 (2012) 357–372.
- [7] A. Marcu, G. Toth, R. Srivastava, P. Strasser, *J. Power Sources* 208 (2012) 288–295.
- [8] M. Oezaslan, F. Hasche, P. Strasser, *J. Electrochem. Soc.* 159 (2012) B394–B405.
- [9] M.K. Debe, *ECS Trans.* 45 (2012) 47–68.
- [10] M.K. Debe, A.K. Schmoedel, G.D. Vernstrorn, R. Atanasoski, *J. Power Sources* 161 (2006) 1002–1011.
- [11] E.A. Ticianelli, C.R. Derouin, A. Redondo, S. Srinivasan, *J. Electrochem. Soc.* 135 (1988) 2209–2214.
- [12] E. Passalacqua, F. Lufrano, G. Squadrito, A. Patti, L. Giorgi, *Electrochim. Acta* 46 (2001) 799–805.
- [13] X. Cheng, B. Yi, M. Han, J. Zhang, Y. Qiao, J. Yu, *J. Power Sources* 79 (1999) 75–81.
- [14] A. Bose, R. Shaik, J. Mawdsley, *J. Power Sources* 182 (2008) 61–65.
- [15] F. Liu, C.Y. Wang, *Electrochim. Acta* 52 (2006) 1417–1425.
- [16] J.M. Song, S.Y. Cha, W.M. Lee, *J. Power Sources* 94 (2001) 78–84.
- [17] H.A. Gasteiger, J.E. Panels, S.G. Yan, *J. Power Sources* 127 (2004) 162–171.
- [18] S. Martin, P.L. Garcia-Ybarra, J.L. Castillo, *Int. J. Hydrogen Energy* 35 (2010) 10446–10451.
- [19] A.M. Chaparro, M.A. Folgado, P. Ferreira-Aparicio, A.J. Martin, I. Alonso-Alvarez, L. Daza, *J. Electrochem. Soc.* 157 (2010) B993–B999.
- [20] S. Martin, P.L. Garcia-Ybarra, J.L. Castillo, *J. Power Sources* 195 (2010) 2443–2449.
- [21] S. Martin, B. Martinez-Vazquez, P.L. Garcia-Ybarra, J.L. Castillo, *J. Power Sources* 229 (2013) 179–184.
- [22] M. Brodt, R. Wycisk, P.N. Pintauro, *J. Electrochem. Soc.* 160 (2013) F744–F749.
- [23] W.J. Zhang, P.N. Pintauro, *ChemSusChem* 4 (2011) 1753–1757.
- [24] J.D. Snyder, Y.A. Elabd, *J. Power Sources* 186 (2009) 385–392.
- [25] H. Chen, J.D. Snyder, Y.A. Elabd, *Macromolecules* 41 (2008) 128–135.
- [26] B. Dong, L. Gwee, D. Salas-de la Cruz, K.I. Winey, Y.A. Elabd, *Nano Lett.* 10 (2010) 3785–3790.
- [27] A. Laforgue, L. Robitaille, A. Mokriani, A. Ajji, *Macromol. Mater. Eng.* 292 (2007) 1229–1236.
- [28] R. Bajon, S. Balaji, S.M. Guo, *J. Fuel Cell Sci. Technol.* 6 (2009). No. 031004-1-031004-6.
- [29] H.A. Gasteiger, W. Gu, R. Makharia, M.F. Mathias, B. Sompalli, in: W. Vielstich, H.A. Gasteiger, A. Lamm (Eds.), *Handbook of Fuel Cells – Fundamentals, Technology and Applications*, vol. 3, 2003, pp. 593–610 (Chapter 46).
- [30] The US Department of Energy (DOE), Energy Efficiency and Renewable Energy, 2011. http://www.eere.energy.gov/hydrogenandfuelcells/mypp/pdfs/fuel_cells.pdf.